- This is the author's peer reviewed, accepted manuscript. However, the online version of record will be different from this version once it has been copyedited and typeset PLEASE CITE THIS ARTICLE AS DOI: 10.1063/5.0171214
- photomultiplier tube assemblies
- Zachary M. Geballe, Francesca Miozzi, Chris F. Anto,^{a)} Javier Rojas, Jing Yang, and

Spectroradiometry with sub-microsecond time resolution using multianode

- 4 Michael J. Walter
- Earth and Planets Laboratory, Carnegie Institution for Science, Washington, DC 20015,
- 6 USA

9

10

11

12

13

14

15

16

17

18

19

20

- 7 (The author to whom correspondence may be addressed: zgeballe@carnegiescience.edu)
- 8 (Dated: 27 December 2023)
 - Accurate and precise measurements of spectroradiometric temperature are crucial for many high pressure experiments that use diamond anvil cells or shock waves. In experiments with sub-millisecond timescales, specialized detectors such as streak cameras or photomultiplier tubes are required to measure temperature. High accuracy and precision are difficult to attain, especially at temperatures below 3000 K. Here we present a new spectroradiometry system based on multianode photomultiplier tube technology and passive readout circuitry that yields a 0.24 μ s rise-time for each channel. Temperature is measured using five color spectroradiometry. During high pressure pulsed Joule heating experiments in a diamond anvil cell, we document measurement precision to be ± 30 K at temperatures as low as 2000 K during single-shot heating experiments with 0.6 μ s time-resolution. Ambient pressure melting tests using pulsed Joule heating indicate that the accuracy is ± 80 K in the temperature range 1800-2700 K.

^{a)}Also at Department of Physics and Astronomy, Johns Hopkins University.

PLEASE CITE THIS ARTICLE AS DOI: 10.1063/5.0171214

I. INTRODUCTION

Pulsed heating in diamond anvil cells (DACs) is useful for measuring thermal conduction, ^{1,2} 22 synthesizing new materials, ^{3–5} creating exotic high density fluids, ^{6,7} and detecting the latent heat 23 of melting. 8 The most common way to measure sample temperatures in pulsed heated DAC exper-24 nents is by fitting a sample's thermal emissions spectra to a greybody function, a method known 25 "spectroradiometry". Together, spectroradiometry and pulsed heating in DACs have enabled 26 everal breakthrough measurements. They were used to document the insulating-to-conducting 27 ransition in fluid hydrogen, 6,7,9 and to measure thermal conductivity of silicates and metals at the 28 pressure-temperature conditions of Earth's lower mantle and outer core. 8,10 Spectroradiometry has 29 also been used to determine temperature during shock wave experiments. 11,12 30

Beyond the experimental challenges in all spectroradiometry measurements, 13-15 two addi-31 tional challenges arise because of the short duration of pulsed heating experiments and shock wave 32 xperiments: the measuring device requires (a) fast time resolution and (b) low enough noise for 33 recise temperature fits. The desired precision is typically in the range of 10 to 100 K. The desired 34 time resolution varies from ns to ms.^{2,6,11,16} 35

The ideal spectroradiometry system would enable high precision measurements at a wide range 36 of temperatures with high time resolution during single shot experiments (i.e., without need to 37 ccumulate signal during multiple experiments). In practice, tradeoffs are necessary. We now 38 focus on studies using DACs. Several DAC studies have shown measurements at temperatures 39 down to \sim 1500 to 1800 K with \sim 10 ns to a few ms time resolution while accumulating thermal 40 emissions for tens to hundreds of ms.^{2,16,17} Ref. 18 extended the low temperature limit using 1 ms 41 me resolution, reaching 1300 K during single shot experiments, and temperature as low as 800 42 during during multi-shot experiments. Refs. 8 and 19 extended the lower limit of cumulative 43 heating duration. They used streak cameras to measure temperatures in the range 3000 K to 13,000 with $\sim 0.5 \,\mu s$ time resolution while accumulating data with 1 to 10 repetitions. 45

In the present study, we extend the lower limit of temperature far below 3000 K while main-46 taining sub- μ s time resolution during single shot experiments. Notably, this opens up the possibility of accurate temperature measurements at conditions typical of Earth's lower mantle (\sim 1800 - 2500 K and 23 - 136 GPa) while performing single shot, μ s-timescale heating experi-49 ments in DACs. We also improve temperature precision relative to our previous work.⁸ Moreover, the cost of the system is reduced substantially compared to optical systems based on expensive PLEASE CITE THIS ARTICLE AS DOI: 10.1063/5.0171214

This is the author's peer reviewed, accepted manuscript. However, the online version of record will be different from this version once it has been copyedited and typeset.

- streak cameras. The key technology is a multianode photomultiplier tube (MA-PMT) assembly.
- 53 MA-PMT assemblies have been used for spectroscopic measurements of chemical kinetics during
- shock experiments.^{20–22} They are a new technology for spectroradiometry in DACs.
- One MA-PMT assembly is installed as the optical detector for spectroradiometry on each side
- of a new optical table at the Carnegie Earth and Planets Laboratory. The table is designed for
- pulsed Joule heating and spectroradiometry of diamond anvil cell samples. In section II, we present
- details of the new optical table. In section III, we show the results of calibrations and tests using
- incandescent lamps and pulsed LEDs. In section IV, we describe the data processing method.
- Section V shows examples of heating at high pressure (~ 76 GPa). Lastly, section VI assesses
- the accuracy of the temperature measurement based on melting tests on four ambient-pressure
- samples: iron, platinum, alumina, and iridium.

63 II. OPTICAL AND ELECTRONIC SETUP

- We divide the description of the new optical table into three parts: the optics, the MA-PMT
- assemblies, and the readout electronics.

66 A. Optics

- The optical table design is shown schematically in Fig. 1 and in a photo in Fig. 2. It bor-
- rows many design attributes and optical component choices from existing laser heating systems
- for diamond anvil cells (DACs), ^{2,23–25} including the following: apochromatic objective lenses to
- collimate the sample's thermal emissions, irises to reduce chromatic aberration, and mirror pin-
- holes at the front of a spectrometer. A CMOS camera monitors the position of the sample image
- on the mirror pinhole.
- Several details of the optical system are different from all eight of the laser heating systems
- described in 2, 23–29. First, each mirror pinhole was fabricated in-house using an RF-magnetron
- sputtering system to deposit a ~ 400 nm thick aluminum film onto the surface of an anti-reflective
- coated piece of optical glass (Edmund Optics 45-658). Before the sputter-deposition, a 100 μm
- diameter disc of platinum was placed at the center of the optical glass as a mask. After sputter-
- deposition, the mask was removed. Appendix A describes masking and sputtering details. Second,
- 79 the main focusing lenses (L3 and L4 in Fig. 1) perform two functions: they focus thermal emis-

PLEASE CITE THIS ARTICLE AS DOI: 10.1063/5.0171214

Oscilloscope Oscilloscope /////// /////// Electronics **Electronics** MA-PMT MA-PMT Spec 2 Spec 1 C1 СЗ C2 C4 MP1 MP2 L8< Iris BS BS Iris BS BS DAC

FIG. 1. Schematic of the optical table. This paper focuses on the optics (black) and the readout electronics for the MA-PMTs (blue). Grey shading indicates the electronics for pulsed Joule heating, which is the topic of the first of the two submitted manuscripts. Objective lenses L1 and L2 (20X Mitutoyo Plan Apo NIR Infinity Corrected) collimate thermal emissions from the diamond anvil cell (DAC). Ten percent of the collimated light is reflected by cube beamsplitters (BS; ThorLabs BS025) and focused by achromatic lenses (L7, L8; ThorLabs AC254-200-AB) onto CMOS cameras (C1, C2; FLIR BFS-PGE-16S2C-CS Blackfly S PoE, Color). The transmitted light passes through irises (Iris; ThorLabs SM1D12C) and cube beamsplitters (same part as above), and is focused by achromatic focusing lenses (L3, L4; ThorLabs AC254-200-AB) onto the mirror pinholes (MP1, MP2; aluminum coated Edmund Optics 45-658) located at the focal positions of the two spectrometers. The images of the sample on the mirror pinholes are reflected back along the incident beam paths to the outer beamsplitters. Ten percent of the mirror-pinhole-reflected image is reflected by cube beamsplitters, focused by achromatic lenses (L5, L6; same part as above) and captured by CMOS cameras (C3, C4; BFS-U3-16S2C-CS USB 3.1 Blackfly S, Color). The light that passes through mirror pinhole is chromatically dispersed by the spectrometers (Holospec VPH with HFG-750 transmission grating on the left side; Acton SP2358 with 150 g/mm grating on the right side). The chromatically dispersed light (shown schematically as a rainbow), is detected by MA-PMT assemblies (Hamamatsu H7260-20). Blue boxes and curves indicate electronics and electrical connections. The schematic does not show the following optical elements that are removed from the beam path during heating experiments: shutters (ThorLabs SH05) located between the focusing lenses and the mirror pinholes, which can be closed to measure background from stray light and/or electrical pickup; white LED illumination can be delivered by pellicle beamsplitters (ThorLabs BP145B1) on electrical flipper mounts (New Focus 8893) located between the objective lenses and cube beamsplitters.

PLEASE CITE THIS ARTICLE AS DOI: 10.1063/5.0171214

91

MA PMT + MA PMT electronics Oscilloscope Spec 1 Electronics

FIG. 2. Photograph of the optical table, with blue labels marking the spectrometers, MA-PMT assemblies, and electronics including oscilloscopes.

sions onto the mirror pinhole, and they collimate light reflected from the mirror pinhole. This 80 design feature saves space on the optical table. Third, we include a second CMOS camera on each 81 side (C1,C2), along with a stationary beamsplitter and a lens (L7,L8) to monitor the entire sample, 82 including the 5 μ m-diameter disc that images onto the pinhole. The images from CMOS cameras 83 1 and C2 during heating are useful for estimating the spatial distribution of sample temperature sing pyrometry (e.g. Fig. S1 of Ref. 30). We use cube beamsplitters rather than pellicle beam-85 splitters because their transmission spectra are much smoother, and because they are less prone to 86 mechanical damage. The downside of cube beamsplitters is that, despite their anti-reflective coat-87 ng, they can create ghost images that can focus onto the mirror pinhole. In the present setup, ghost 88 nages were avoided by rotating each cube beamsplitter 3° away from the optical axis, causing 89 reflections from the cube surfaces to avoid all the nearby reflective surfaces on our table. 90

The two spectrometers were repurposed from previous experimental setups. The left side uses Holospec VPH spectrometer equipped with a HFG-750 transmission grating. The right side 92 ses an Acton SP2358 spectrometer equipped with a 150 g/mm grating blazed at 500 nm. The ravelength ranges detected on the left and right sides are approximately 450-850 nm and 400900 nm, respectively. A more symmetric design to achieve a similar bandwidth with a smaller footprint would use 150 mm focal length reflecting spectrometers with 300 g/mm grating on each

PLEASE CITE THIS ARTICLE AS DOI: 10.1063/5.0171214

97 side.

98 B. MA-PMT assemblies

Thermal emissions are detected on each side of the DAC sample using a multi-anode photomultiplier tube (MA-PMT) assembly (Hamamatsu H7260-20). Each MA-PMT assembly consist of a linear array of 32 photomultiplier tubes with hard-wired voltage dividing circuitry. Similar MA-PMT assemblies are used in the shock-wave spectroscopy systems of Refs. 20 and 21. In our setup, the package is housed in a 10x10x3 cm aluminum holder that is attached to either the spectrometer itself (for the Acton spectrometer) or to a motorized linear translation stage positioned in front of the spectrometer output (for the Holospec spectrometer).

Each MA-PMT assembly is powered by a high voltage power supply (SRS PS325 and SRS PS310 for left and right sides, respectively). In practice, we operate the power supplies in the range -500 V to -900 V, which corresponds to gains in the range 10^4 to 3×10^6 .

OPPOSITE SECTION 1999 C. MA-PMT readout electronics

The outputs of the 32 MA-PMT channels are bunched into 6 groups of 5 for the Holospec 110 spectrometer on the left side of the optical table, and 7 groups 4 for the Acton spectrometer on the 111 right side of the optical table, leaving some unused. Each group of outputs is combined electrically 112 and shunted to ground through a 2.5 k Ω resistor, as shown schematically in Fig. 3. The unused 113 PMT outputs are grounded. Output voltage is measured by 10x oscilloscope probes connected 114 to 8-channel oscilloscopes. The choice of 2.5 k Ω resistance is low enough to yield sub- μ s time 115 resolution and high enough so that ~ 2000 K metal samples produce voltages in most oscilloscope 116 channels that are several orders of magnitude above the 2 μ V quantization noise of the oscillo-117 scope. (The exceptions are the bluest channel and farthest infrared channel, which usually do not 118 detect signal above the noise, leaving five usable oscilloscope channels out of seven. For the right 119 side, very low quantum efficiency of the MA-PMT likely explains the low signal in the reddest 120 channel, while a combination of low quantum efficiency and low intensity of our greybody sources 121 likely explains the low signal on the bluest channel. The low signals on the left side have similar 122 origins, in addition to possible vignetting inside the spectrometer.)

PLEASE CITE THIS ARTICLE AS DOI: 10.1063/5.0171214

125

126

127

128

129

130

131

132

BNC 2.5 panel 8 Ch kOhm 10x resistors scope probes 32 channel PMT array Supply Trigger from voltage pulse generator

FIG. 3. Schematic of the MA-PMT assembly and readout electronics used on the right side of the optical table. Counterclockwise from bottom left: a supply voltage from a high voltage power supply (SRS PS310) sets the gain on the 32-channel MA-PMT assembly (Hamamatsu H7260-20). Seven sets of four PMT anodes are electrically connected. Each set of anodes is shunted to ground through a 2.5 k Ω resistors (1% accuracy, 1/8 W), and connected via a BNC panel mount to a 10x oscilloscope probe (ProbeMaster 6143-4), which is connected to one channel of an 8-channel oscilloscope (Picoscope 4824A; 20 MHz, 12-bit). One channel of the oscilloscope is required to receive the trigger from a pulse generator.

CALIBRATION AND MA-PMT CHARACTERIZATION

The MA-PMT assemblies are the major difference in this optical table compared to previous spectroradiometry systems for pulsed laser heating and pulsed Joule heating.^{2,17,23,24} Four key challenges in using a MA-PMT assembly are: (1) to ensure data is collected in the linear regime of the MA-PMT assembly, (2) to ensure a desirable combination of time resolution, wavelength resolution, and noise floor, (3) to calibrate the wavelength range of each readout channel, and (4) to apply sufficient grounding so that MA-PMTs and their readout electronics are negligibly affected by the Joule heating pulse - a challenge that is specific to pulsed Joule heating. Below, we describe the results of tests for each of these challenges, plus a system response measured with a NIST-traceable tungsten lamp to calibrate the spectroradiometric measurements.

PLEASE CITE THIS ARTICLE AS DOI: 10.1063/5.0171214

135

136

137

138

139

140

141

142

143

144

145

10^{2} 900 V 10^{-1} 800 V 10^{1} 700 V 10⁻² 600 V Julse magnitude (V) 10⁰ 500 V Anode current (A) 400 V 10⁻³ 300 V 10^{-4} 10^{-2} 10⁻⁵ 10^{-3} 10⁻⁶ 10^{-4} 10^{-7} 10^{-5} 10^{0} 10^{-3} 10^{-2} 10^{-1} LED intensity (arb.)

FIG. 4. Linearity testing results. Circles and solid curves show the amplitude of the PMT measurement of a 20 µs pulse from a high-powered green LED (Luminus SBT-70-G) on the right side of the optical table using variable gain (different colors), and variable attenuation (horizontal axis). Pulse amplitude is recorded from the channel 4 of the oscilloscope, which measures wavelength in the range 530-600 nm. Dashed lines show a linear response (i.e. slope = 1 in log-log space). The legend lists the voltages used to set the gain of the MA-PMT assembly.

MA-PMT Linearity 134

The range of anode currents over which a PMT is linear depends strongly on the pulse duration. 3132 Our system is designed for pulse durations in the range ~ 1 to 100 μ s. Fig. 4 shows that at 20 μ s pulse duration, one of the central channels of the detector is approximately linear up to ~ 0.4 mA (100 mV) at -700 to -900 V supply voltages. The data at lower supply voltages remains linear up to the highest light levels tested. The anode current is linear down to at least 0.1 μ A at -500 V supply voltage. Our measurements at lower anode currents are not precise enough to test linearity. The $\sim 0.1~\mu A$ - 0.4 mA range documented here is meant only as a guide, because the effect of non-linearity on spectroradiometry is a complicated function of temperature-time history and supply voltage. Below, we use a different test to show that anode non-linearity does not affect our measured temperatures during Joule heating experiments. We vary supply voltage in the range -550 to -800 V (hence varying anode current 30-fold) and show that the change in fitted temperature is within the scatter of temperature measurements. Appendix

PLEASE CITE THIS ARTICLE AS DOI: 10.1063/5.0171214

154

155

156

157

B describes how the choice of MA-PMT assembly and its optical focusing procedure may affect linearity.

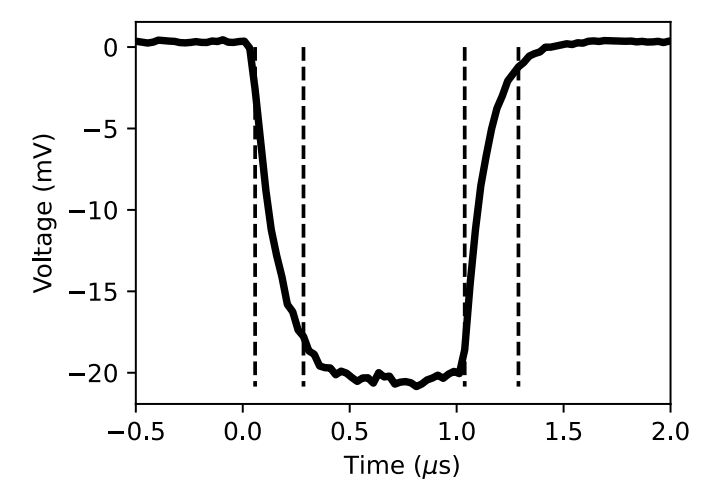
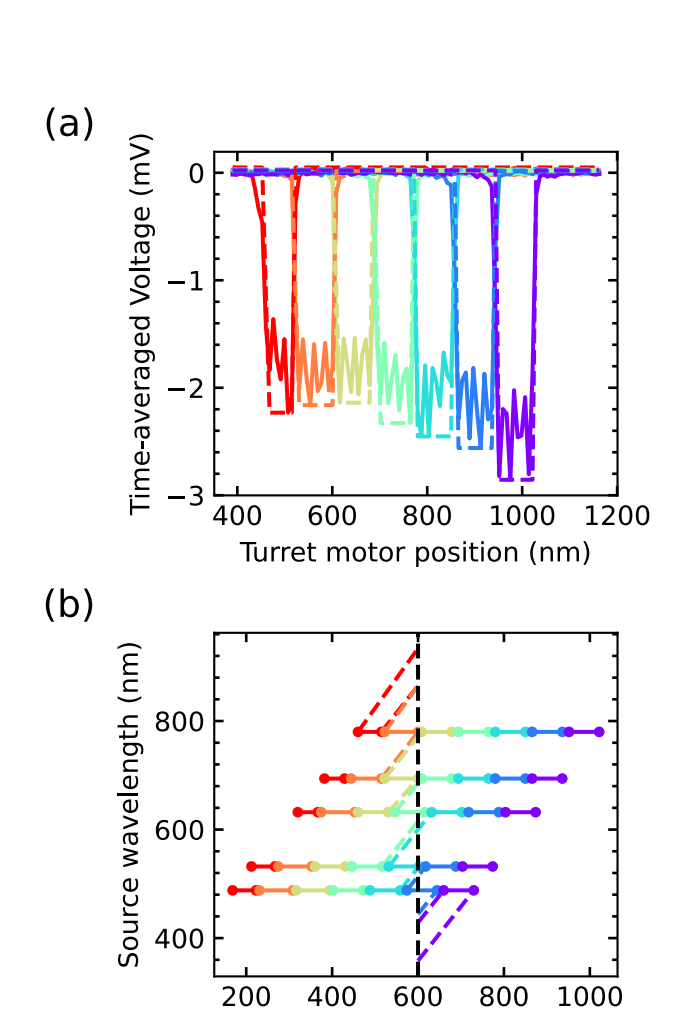


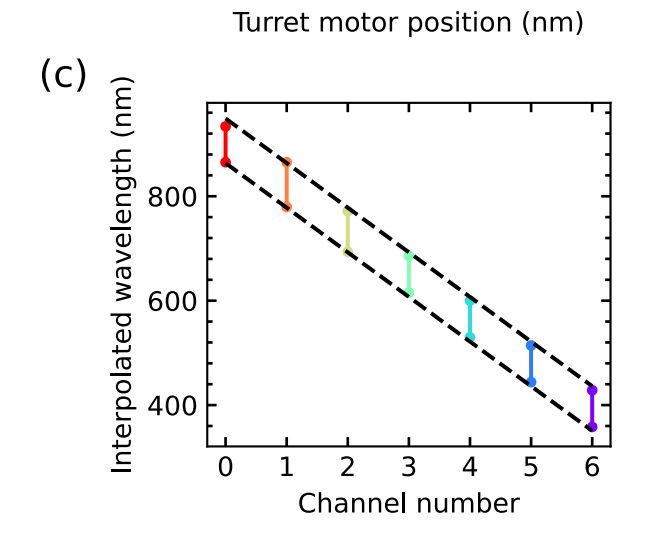
FIG. 5. Time resolution. The black curve is channel 3 (620-690 nm) of the right side of the optical table, measured while pulsing a red LED (ThorLabs LED630L) using a 1 μ s square wave output from a pulse generator (Berkeley Nucleonics 525). Vertical dashed lines mark 10% and 90% of the full rise and fall. The rise and fall times are 0.23 μ s and 0.25 μ s.

Time resolution 149

We measure the time resolution of our detector by measuring the response to a red LED that is 150 driven by a 1 µs square wave from a pulse generator. Fig. 5 shows that the typical rise time and 151 fall time is $0.24 \pm 0.1 \,\mu$ s. Here we define rise and fall times by the times that the signal reaches 10 152 and 90% of the pulse magnitude, a definition that corresponds to 2.2RC for an ideal circuit made 153 up of a single resistor with resistance R and a single capacitor with capacitance C. This suggests that the total capacitance per oscilloscope channel is $C = 0.24 \,\mu\text{s}/2.2/2.5\text{k}\Omega = 40 \,\text{pF}$. (The total capacitance is the sum of each electrical lead self capacitance and the output capacitances of four PMT anodes). Further testing with shunt resistances in the range 1-10 k Ω confirms that the rise time and fall time of the detector varies in proportion to the value of shunt resistance.

This is the author's peer reviewed, accepted manuscript. However, the online version of record will be different from this version once it has been copyedited and typeset. PLEASE CITE THIS ARTICLE AS DOI: 10.1063/5.0171214





PLEASE CITE THIS ARTICLE AS DOI: 10.1063/5.0171214

160

161

162

163

164

165

166

167

168

169

170

171

172

173

174

175

176

177

178

FIG. 6. Wavelength calibration for the right side spectrometer and MA-PMT assembly. (a) Time-averaged voltages (solid curves) and best-fit square wave (dashed curves) for each oscilloscope channel (colors) when the mirror pinhole is illuminated by 780 ± 5 nm light, plotted as a function of the motor position of the spectrometer's turret. (b) A summary of the square-waves fitted to data from (a) and the analogous data for 488, 532, 632, and 694 nm light. Circles and line segments mark the ranges where fitted square waves are less than 0. Dashed colors mark linear interpolations and extrapolations of the circles. The motor position used in experiments is marked by the vertical dashed black line at 600 nm. (c) The locations of linear interpolations and extrapolations to 600 nm motor position from (b) are marked as colored circles. Black dashed lines show the final wavelength calibration, a linear fit to channels 1-6.

Wavelength calibration 159

Wavelength calibration with a MA-PMT assembly presents a subtle challenge. A calibration is required because the relative alignment of detector and spectrometer affects the wavelengths detected on each channel. (Note that this is unlike previous DAC studies such as Refs. 16 and 18 in which notch filters are used to separate colors). And yet there are not enough channels to use a high spectral resolution standard source like a neon lamp that is typical when calibrating a CCD detector. Finally, we do not directly measure the wavelength range detected by each channel because we do not own continuously tunable monochromatic light sources (e.g. a set of tunable dye lasers).

Rather than calibrating channels directly, we use a three-step analysis procedure based on intensity data collected as a function of motor position, where the motor scans the MA-PMT assembly with respect to the location of a narrow bandwidth of light. First, we illuminate the pinhole of the spectrometer with a 10 nm band of light (e.g. 532 ± 5 nm) by backlighting a 10 nm bandpass filter with an incandescent lamp. We then use a motor to scan the position of the MA-PMT assembly relative to the narrow band of light. On the Holospec side, we use a linear motor to translate the MA-PMT assembly. On the Acton side, we use the spectrometer's turret motor to move the narrow band of light. An example of the resulting intensity scan on the Acton side is shown in Fig. 6a. The first analysis step is to identify the range of motor positions for which the light is detected by each channel of the MA-PMT detector, ignoring any channels that are not fully transited by the motor scan. Here, "detected" means that the measured voltage is at least half its maximum value during the scan. We perform this procedure for each of the following

PLEASE CITE THIS ARTICLE AS DOI: 10.1063/5.0171214

bands of light: 488 ± 5 nm, 532 ± 5 nm, 632 ± 5 nm, 694 ± 5 nm, 780 ± 5 nm. Fig. 6b shows the 180 range of motor positions plotted versus the central wavelength of the light source for each channel. 181 Note that our incandescent light and set of bandpass filters could be replaced with alternative light 182 sources that provide even narrower bandwidth, such as a set of lasers. The likely result would be 183 even sharper transitions from "detected" to "not detected". For this study, however, the transitions 184 appear to be sufficiently sharp for easy identification of wavelength ranges (Fig. 6a). 185

The second analysis step is linear interpolation and extrapolation to the motor position that is 186 used for experiments. We use the "600 nm" position of the Acton turret motor in our experiments. 187 The interpolations and extrapolations are shown as dashed lines in Fig. 6b. Linear extrapolation is 188 reasonable since the spectrometer grating dispersion is nearly linear, and since the photocathodes 189 in the MA-PMT assembly are evenly spaced. Finally, we fit the central wavelengths of channels 190 1-6 of the Acton side and channels 1-4 of the Holospec side to a linear function. We use this linear 191 function as our wavelength calibration. 192

System response

The "system response" of each side of the optical table is the wavelength-dependent function 194 that describes the voltage generated at the oscilloscope per photon emitted at the sample position. 195 It is the wavelength-dependent transmission of all optics times the efficiency of the MA-PMT as-196 sembly and readout electronics in converting photons to volts. We follow the typical procedure 197 for spectroradiometry, placing the filament of a NIST-traceable tungsten lamp at the sample po-198 sition. We use 500 mA to heat the single-loop tungsten lamp described in Ref. 33 to the color 199 temperature T = 2255 K. We set the supply voltage of the left and right MA-PMT assemblies to 200 -650 and -700 V in order to achieve a sufficiently low anode current (< 10 μ A) to avoid non-201 linearities, which occur around 15 μ A when illuminating with continuous light. The resulting 202 system response for left and right sides are plotted in Fig. 7a,b. 203

Electrical pickup 204

A spurious signal is generated in raw PMT voltages due to electrical pickup of large pulses of 205 Joule heating current. For example, Fig. 8a shows the result of a ~ 10 A, 100μ s pulse of electric-206 ity through a platinum sample. The dominant signal in Fig. 8 is caused by thermal emissions as 207

PLEASE CITE THIS ARTICLE AS DOI: 10.1063/5.0171214

208

209

210

211

212

213

214

215

(a) (b) $B(2255 \text{ K}) (\text{W sr}^{-1} \text{ m}^{-2})$ B(2255 K) (W sr^{−1} 0 $V_{\rm W}$ (mV) 50 V_w (mV) 100 100 150 150 -3 ' nm⁻¹) 0.00 M (mV W⁻¹ sr m² nm) 0.00 M (mV W⁻¹ sr m² nm) -0.02 -0.05-0.04-0.10-0.06 -0.15 400 600 800 600 800 400 Wavelength (nm) Wavelength (nm)

FIG. 7. System response on left (a) and right (b) sides. (Top row) Time averaged voltage measured $(V_{\rm W},$ solid black) and interpolated ($V_{W,\text{interp}}$, dashed black). The measurement uses a tungsten lamp heated to 2255 K color temperature and supply voltages -650 V and -700 V on left and right sides, respectively. The blackbody function B(2255 K) is plotted in red. (Bottom row) A visual representation of the system response matrix, $M = V_{W,interp}/B$. Each color corresponds to a row of the matrix. Each wavelength corresponds to a column of the matrix. In this figure, the oscilloscope channels are divided into 4 wavelengths for ease of visualization; 100 divisions per channel are used during analysis. For comparison, the black rectangles show the naive ratio calculated at the central wavelength, $V_{\rm W}(\lambda_i)/B(2255~{\rm K},\lambda_i)$.

the sample heats to ~ 2000 K, a relatively low temperature. The spurious signal is the ~ 1 mV oscillation with period $\sim 200~\mu s$. The spurious signal scales with current amplitude, and occurs even when the optical shutter is closed or when the sample is replaced by a dummy resistor, indicating that it comes from electrical pickup. The spurious pickup signal is approximately independent of oscilloscope channel, allowing us to use an edge channel (channel 0 or 6) from each oscilloscope as the background (e.g. Fig. 8b). (An alternative scheme for even better accuracy is to subtract background curves for each channel with the optical shutter closed). See Appendix C for further details.

PLEASE CITE THIS ARTICLE AS DOI: 10.1063/5.0171214

(b) (a) 0.0 Voltage (mV) Voltage (mV) -2.5 -5.0 -7.5-200 0 100 200 100 200 Time (µs) Time (µs)

FIG. 8. An example of the correction for electrical pickup in raw oscilloscope traces. (a) Raw traces for each channel on the left side of the optical table during pulsed heating of platinum to 2000 K using a current pulse that peaks at 10 A. The MA-PMT assembly supply voltage is -850 V. (b) Traces after subtracting the channel plotted in purple. The channel is not connected to the MA-PMT assembly, but rather measures spurious pickup induced through the 10x probe and 2.5 k Ω resistor.

DATA PROCESSING

Time-resolved temperature is inferred using the following two-step method, which is similar to 217 the methods in Refs. 2 and 8: 218

Step 1 of temperature analysis: a single two-parameter fit

A two parameter fit for temperature (T) and emissivity (ε) is performed for voltage data aver-220 aged across a time interval of interest. In the example shown in Fig. 9, we choose the time-interval 221 5.0 - 5.5 μ s, with time measured from the beginning of the electrical pulse. The thermal emis-222 sions are averaged over the time-interval of interest and over all pulse repetitions, yielding a single 223 spectrum, V_i . Here, i denotes a channel of the oscilloscope, which corresponds to a band of wavelengths. 225

The measured spectrum is fit to a greybody function multiplied by the system response ma-226 trix, M, and integrated over wavelength:

14

$$V_i = \varepsilon \int M(i,\lambda)B(T,\lambda)d\lambda \tag{1}$$

PLEASE CITE THIS ARTICLE AS DOI: 10.1063/5.0171214

254

233

234

Here, *B* is Planck's blackbody function:

$$B = \frac{2hc^2}{\lambda^5} \frac{1}{e^{\frac{hc}{\lambda k_B T}} - 1} \tag{2}$$

where c is the speed of light, h is Planck's constant, k_B is Boltzmann's constant, and λ is wavelength. The system response matrix is defined by

$$M(i,\lambda) = \frac{V_{\text{W,interp}}}{B(2555 \text{ K},\lambda)} \text{ if } \lambda_i - \delta \lambda / 2 < \lambda < \lambda_i + \delta \lambda / 2$$
 (3)

$$= 0 \text{ otherwise}$$
 (4)

Temperature (T) and emissivity (ε) are the two free parameters. Variables λ_i and $\delta\lambda$ denote 235 the center and bandwidth of the measured wavelength band. The wavelength-dependent volt-236 age, $V_{W,interp}$, is an interpolation of the voltage, V_{W} , that is measured during calibration with a 237 standard tungsten lamp heated to a color temperature of 2255 K. See Appendix D for interpolation 238 details. The top panels in Figs. 7a,b show $V_{\rm W}$ (solid black), $V_{\rm W,interp}$ (dashed black), and $B(2255~{\rm K})$ 239 (red), while the bottom shows the system response matrix, M. Note that interpolation is required 240 to achieve accuracy < 50 K in this study, because the bandwidth of each oscilloscope channel 241 ~ 80 nm. For comparison, spectroradiometry using a CCD or streak camera does not require 242 interpolation because intensities are measured over narrow wavelength bands; a single pixel typically detects ~ 0.5 nm. In those cases, the system response matrix is replaced by the normal system response. As another comparison, Ref. 16 uses a different type of interpolation to account for the ~ 40 nm wide bands used in their PMT spectroradiometry setup: interpolation of voltage versus temperature from a tungsten lamp heated to a wide range of temperatures (Fig. 3 of Ref. 247 16). 248

We find the best fit values of ε and T by fitting (1) with the "optimize.curve_fit" function within the scipy library in python. We estimate relative uncertainties in the fitted data, dV/V, as the inverse square root of the absolute value of measured voltage, $|V_i|^{-0.5}$, in order to account for shot noise in the photocathode of the MA-PMT assembly. (I.e., we set "absolute_sigma = False" and sigma = $|V_i|^{-0.5}$ in optimize.curve_fit).

B. Step 2 of temperature analysis: a series of one-parameter fits

The second step in our temperature analysis is a one parameter fit to the total measured voltage, assuming the best fit emissivity from step 1. We numerically solve the following equation for temperature, T, at each time, t:

This is the author's peer reviewed, accepted manuscript. However, the online version of record will be different from this version once it has been copyedited and typeset PLEASE CITE THIS ARTICLE AS DOI: 10.1063/5.0171214

Before plotting, we typically smooth the curves T(t) using a Savitkzy-Golay filter with polynomial order 2 and timescale, τ , that is at least 5 times smaller than the pulse duration (e.g. $\tau = 0.6 \,\mu$ s for the 5 μ s pulse in Fig. 9). In all cases, we plot the filtered values of T(t) in colors. In some cases, we plot the unfiltered T(t) curves in grey (e.g. Fig. 9).

55 V. RESULT FROM A HIGH PRESSURE JOULE-HEATED SAMPLE

To demonstrate the utility of the optical table and MA-PMT detectors for high pressure experiments, we show examples of temperature measurements during pulsed Joule heating of an iron sample compressed in a KCl pressure medium in a DAC to \sim 70 GPa at 300 K and heated to \sim 2800 K. Joule heating is performed by the method described in the first of the two submitted manuscripts. Pressure is measured by X-ray diffraction and by the diamond anvil Raman edge.³⁴

Results of the temperature analysis for data accumulated during four different experiments are shown in Fig. 9. In one experiment, a single heating pulse is recorded. In the others, thermal emissions from repeated pulses are accumulated 10, 100, or 1000 times. In all cases, the T(t) curves show outstanding reproducibility – the peak temperature varies by less than ± 30 K on each side of the sample. The T(t) curves show similarly small scatter down to low temperatures, reaching ~ 2000 K for the single shot data and ~ 1700 K for the 1000 repetition data.

The outstanding signal to noise at temperatures below 3000 K suggests a major improvement compared to our previous study using a streak camera, a study that itself pushed the limits of low temperature ($T \sim 3000$ K) for DAC heating experiments with high time resolution ($\sim 0.6~\mu s$) and few repetitions (1 to 10). Fig. 10 compares examples from Fig. 9g with one of the most precise and reproducible data sets from Ref. 8, the platinum melting data at ~ 68 GPa. The comparison shows that the precision and shot-to-shot reproducibility documented here at ~ 2000 K is approximately equal to that documented in Ref. 8 at ~ 3000 K.

Since non-linearity in a PMT response would appear as an insidious smooth function (as opposed an easy-to-detect flat distribution of saturated counts on a CCD), it is important to verify that the thermal emissions data is collected using a gain where the MA-PMT response is sufficiently

This is the author's peer reviewed, accepted manuscript. However, the online version of record will be different from this version once it has been copyedited and typeset. PLEASE CITE THIS ARTICLE AS DOI: 10.1063/5.0171214

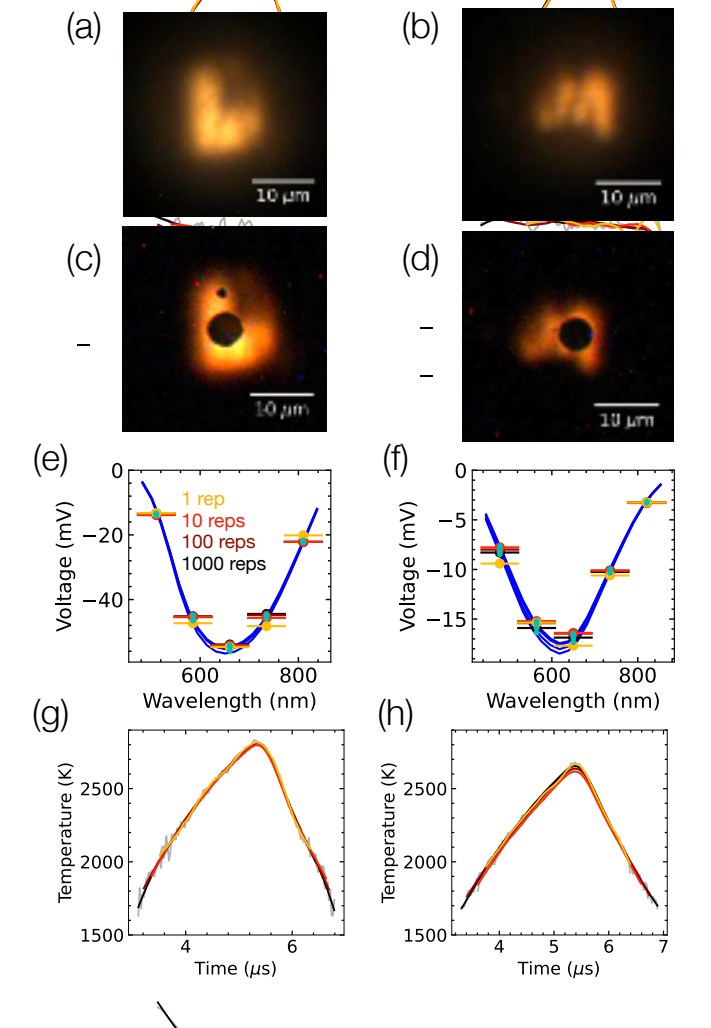


FIG. 9. Photographs and temperature measurements for four pulsed-Joule heating experiments of iron at \sim 76 GPa. The left and right columns show data from the left and right sides of the optical table, which collect thermal emissions from the cylinder-side and piston-side of the DAC, respectively. (a-d) Photographs of the cumulative thermal emissions during 100 heating repetitions, viewed directly in CMOS cameras C1 and C2 (a and b), and after reflection off the mirror pinhole in CMOS cameras C3 and C4 (c and d). (e, f) Wavelength-dependence of MA-PMT voltages from thermal emissions collected during the time period 5– 5.5 \(\mu\)s during a set of 1000 heating repetitions (black circles), 100 heating repetitions (dark red circles), 10 heating repetitions (bright red circles), and 1 heating repetition (yellow circles). Horizontal line segments indicate the width of wavelength bands. Blue curves and cyan dots represent the best fit temperature and emissivity, with blue curves marking the integrand in equation 1, $MB(\varepsilon,T)$ and cyan dots showing the average value of $MB(\varepsilon,T)$ across each band of wavelengths. (g, h) Temperature evolution during each set of heating experiments. The filter timescale is $0.6 \mu s$.

This is the author's peer reviewed, accepted manuscript. However, the online version of record will be different from this version once it has been copyedited and typeset. PLEASE CITE THIS ARTICLE AS DOI: 10.1063/5.0171214

287

288

289

290

291

292

293

294

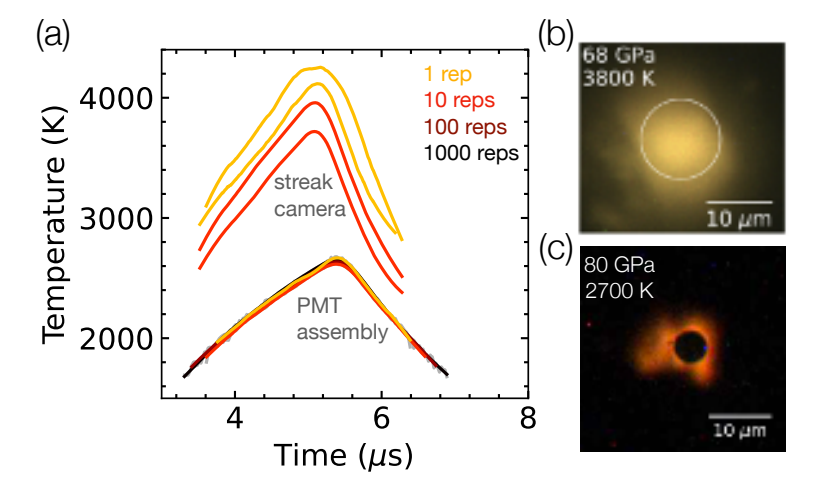


FIG. 10. Streak camera versus a MA-PMT assembly. (a) A comparison of temperature evolution of a platinum sample heated to ~ 4000 K, 68 GPa, based on the streak camera measurements in Ref. 8 versus the temperature evolution of the ~ 80 GPa iron sample heated to 2800 K using a MA-PMT assembly in this study. The platinum curves are newly processed temperature fits using the same data set used to generate Fig. 6 of Ref. 8. Here, we fit temperatures at a wider range of times – the maximum time range possible without fitting noise and generating ~ 1000 K scatter. The iron curves are identical to those in Fig. 9 of this study. In both cases, the filtering timescale is $0.6 \mu s$. (b) Image of the hot platinum sample used to generate the streak camera curves in (a). The white circle marks the region of sample whose emissions are collected on the streak camera. (c) Image of the hot iron sample used to generate the "MA-PMT assembly" curves in (a), reflected off a mirror pinhole.

linear to avoid systematic error larger than the claimed precision (± 30 K). Indeed, temperature measurements on high pressure iron are independent of the gain of the MA-PMT assembly within a 30-fold range of gain, for both left and right side. On the right side, there is no detectable gaindependence for supply voltages above -600 V, within the ± 20 K scatter (Fig. 11f). On the left side, there is gain-dependence to peak temperature within the range -550 to -800 V (Fig. 11e), corresponding to averaged PMT voltages in the range -8 to -200 mV, a 30-fold range. Above -800 V, the non-linear response of the PMT at high anode current degrades accuracy, causing anomalously low temperature fits by up to 60 K at -900 V. Below -550 V, the thermal emissions data becomes very noisy. 295

PLEASE CITE THIS ARTICLE AS DOI: 10.1063/5.0171214

297

298

299

300

301

302

(a) (b) 0.00 Vavg (V) Vavg (V) -0.2-0.05 -0.4-0.105 Time (μs) 5 Time (μs) 6 6 4 (C)(d)2800 2800 Temperature (K) Temperature (K) 2600 2600 2400 2400 2200 2200 2000 2000 5 6 5 (e) Time (µs) (f)Time (µs) Peak temperature (K) Peak temperature (K) 2660 2800 2775 2750 600 800 800 - V_{PMT} (V) - V_{PMT} (V)

FIG. 11. Gain-dependence of temperature fits. Temperature measurements on the left and right sides of the optical table are shown in the left and right columns. The sample is the same high pressure iron sample documented in Fig. 9 but with a higher heating power. (a, b) Average MA-PMT voltages on each side during 31 heating experiments using variable MA-PMT gain. (c, d) Fitted temperatures versus time. The first 30 experiments were conducted with increasing supply voltage from -450 V to -900 V (black to yellow) yielding a \sim 100-fold variation in MA-PMT gain. The 31st experiment (yellow) was collected at -650 V to test for any irreversible changes in the sample. (e, f) Peak temperature versus MA-PMT supply voltage.

AMBIENT PRESSURE MELTING TESTS

We use ambient pressure melting experiments to test the accuracy of spectroradiometric temperature measurements using the new optical table and MA PMT-based detectors. We report tests of four materials that melt in the range 1808 – 2719 K: iron, platinum, alumina, and iridium.

In all cases, melting is detected by unambiguous plateaus upon heating to temperatures at or above the melting temperature. An example is shown in Fig. 12 where several platinum melting experiments are documented. Upon heating, the temperature evolution on each side is nearly linear

Voltage (mV) Voltage (mV) -40 20 -60 -30 -80 200 ō 100 100 200 0 Time (µs) Time (µs) (C)(d)0 Voltage (mV) Voltage (mV) -20 -30 600 800 600 800 Wavelength (nm) Wavelength (nm) (e) (f) 2200 2200 Temperature (K) Temperature (K) 2000 2000 PLEASE CITE THIS ARTICLE AS DOI: 10.1063/5.0171214 Freezing Melting 1800 Freezing 1600 1600 50 50 100 150 100 Time (µs) Time (µs)

(a)

FIG. 12. Melting and freezing of a platinum sample at $P \approx 1$ atmosphere. The sample is a wire of platinum (Alfa Aesar 10292, 25 μ m diameter, 99.95% Pt) that is pressed between $\sim 50~\mu$ m-thick layers of KCl which are pressed gently between diamond anvils (i.e. a DAC with no gasket, compressed to less than 1 GPa of pressure). Left and right columns show data from the left and right sides of the optical table. (a, b) Oscilloscope traces after subtracting the spurious electrical pickup. The rainbow of colors indicates the spectral bands measured in the oscilloscope, matching Fig. 6, from orange at ~ 800 nm to blue at ~ 550 nm. (c, d) Circles show the measured voltage spectrum averaged over the time range 67-75 μ s. As in Fig. 9, horizontal line segments indicate the width of wavelength bands. The cyan dots and blue curves show the values of voltage for the best fit temperature and emissivity. Cyan dots show the average across each wavelength band, while blue curves show the continuous spectrum of voltages, $MB(\varepsilon, T)$. Fit parameters and uncertainties on left (c) and right (d) are $T=2025\pm31$ K, $\varepsilon=0.42\pm0.07$, and $T=2029\pm32$ K, $\varepsilon=0.42\pm0.07$ 0.29 ± 0.05 . (e, f) Temperature versus time. Arrows point to plateaus caused by the latent heat of fusion upon melting and freezing. Dashed lines mark the literature value of platinum's ambient pressure melting temperature, 2040 K. Ten repetitions are averaged. The filter timescale is 10 μ s.

(b)

PLEASE CITE THIS ARTICLE AS DOI: 10.1063/5.0171214

312

313

314

315

316

317

318

319

320

321

322

323

324

325

326

327

328

329

330

331

332

333

before plateauing during the time interval 67-75 μ s. Each side plateaus at a temperature within 20 K of the known melting temperature of platinum, 2040 K. 304

After the melting plateau, the temperature on each side increases by ~ 200 K, and decreases 305 sharply after the current pulse ends. Upon cooling, the temperature on each side again plateaus 306 at approximately the same temperature as the heating plateau. The heating plateaus are caused by 307 absorption of the latent heat of fusion; the cooling plateaus are caused by the release of the latent 308 heat of fusion. Since supercooling of fluids is a much more common phenomenon than super-309 heating of solids,³⁵ we focus on the melting plateaus. For example, in step 1 of the temperature 310 analysis, we use the melting plateau at 67-75 μ s as the time-interval of interest. 311

While it is tempting to also interpret the best fit values of emissivity at melting, in most cases, the fitted value of emissivity includes an error of order 10s of percent caused by the system response calibration. We typically calibrate the system response at a different gain than the measurement – a difference that is often required because of the differing ranges of linearity in pulsed versus continuous PMT measurements. We correct the system response for an approximate gain function that leaves a residual uncorrected gain of order 10%: $V_{W,corrected} = V_W \times 10^{-\Delta V_{PMT}/140 \text{ V}}$ where ΔV_{PMT} is the difference in MA-PMT supply voltage between tungsten lamp and sample measurements.

The same platinum sample from Fig. 12 was melted repeatedly. Fig. 13a,b documents repetitions of the melting measurements. The range of melting plateaus is 2022 ± 10 K and 2020 ± 25 K on the left and right sides of the optical table (shaded grey regions). Figs. 13(d,e) show two other platinum samples that were melted at ambient pressure. Those two samples were pieces of 50 or 25 μ m-diameter wire pressed into thinner copper electrodes and melted in air (i.e., we did not use KCl medium or a DAC to hold the sample). The discrepancy with respect to the 2040 K melting temperature of platinum are slightly greater for these samples (+35 K and +60 K, rather than -20 K for the sample in KCl).

Note that no plateau is detected near the 1793 K ambient pressure boiling temperature of KCl in Figs. 13a,b. The absence of a plateau could be due to the limited amount of heat conducted into the KCl during the heating pulse, and/or due to the blurring of any plateau by the range of equilibrium boiling temperatures that are samples as the KCl pressure changes during the boiling

For ambient pressure melting experiments on metals in air or in vacuum, a wire of the desired metal was pressed into a copper clad board previously divided into a negative and positive side by

PLEASE CITE THIS ARTICLE AS DOI: 10.1063/5.0171214

335

336

337

338

339

340

341

342

343

(b) (d) (a) (C)20 µm 20 µm 2200 Temperature (K) 1800 1600 100 150 50 50 100 150 200 400 600 100 150 Time (µs) Time (µs) Time (µs) Time (µs)

FIG. 13. Melting and freezing of platinum samples at $P \approx 1$ atmosphere. (Top) Images of hot samples on mirror pinholes during individual melting experiments. The black circle in the middle of each image is a mirror pinhole. The small black spot above the mirror pinhole in (a) is an imperfection in the mirror. (Bottom) Temperature evolution during multiple heating experiments on each sample. Each color from black to yellow represents one set of heating experiments. Dashed lines mark the literature value of platinum's ambient pressure melting temperature, 2040 K. Grey shading marks our estimate of plateau temperature. (a,b) Data from the left and right sides of the same sample shown in Fig. 12 – platinum trapped between layers of KCl, 10 repetitions per measurement, filtering timescale 10 μ s. (c) Data from a piece of 50 μ m-diameter platinum wire heated in vacuum, using a single pulse of current (i.e. 1 repetition). The filtering timescale is 20 μ s. (d) Data from a piece of 25 μ m wire heated in air, using a single pulse of current. The filtering timescale is 15 μ s.

cutting a narrow trench with a razor blade. The pressing action was created by using our hands to firmly clamp down on a diamond cell equipped with anvils with 1 mm culets (or in some cases, 0.5 mm culets). Pressing for a couple seconds and then releasing was sufficient to fix the metal in place for iridium. For the relatively soft platinum and iron samples, a thin solder coating was added on top of the copper before pressing the sample. No adhesive was used to fix the wires. Examples of the ambient pressure samples are in Fig. 14.

The data for melting of iridium, iron, and alumina are shown in Figs. 15, 16, 17. The iron and one of the iridium samples were mounted on a copper clad board and inserted into a vacuum chamber with glass viewports. (System response calibration with and without the glass viewport

PLEASE CITE THIS ARTICLE AS DOI: 10.1063/5.0171214

347

348

349

350

351

352

353

354

(a) (b) (c)

FIG. 14. Examples of ambient pressure samples. (a) A platinum sample fixed between anvils with 1 mm culets, no gasket, and KCl insulation. Corresponding data is in Fig. 12. (b) A platinum sample pressed onto a copper clad board that is coated in a thin layer of solder. Anvils were used to press the platinum into the solder, and then removed, leaving the platinum embedded in the solder. Corresponding data is in Fig. 13c. (c) The rhenium capsule filled with alumina, welded shut, and clamped between pieces of molybdenum foil. Corresponding data in Fig. 17d,e.

showed no measurable difference in spectral shape). The iridium samples were cleaved from a piece of iridium wire (Alfa Aesar 11430, 99.8% Ir, 0.5 mm diameter). The iron sample was a 345 piece of 25 µm diameter iron wire (Goodfellow 030-530, 99.99% Fe). 346

The alumina samples were placed inside or on top of a rhenium heater, and held inside the vacuum chamber during heating. In the first experiment, a rhenium heater was constructed from a flattened piece of 100 μm-diameter rhenium wire (Alfa Aesar 10310-BU, 99.97%), which was clamped between pieces of brass. The brass clamp was made by soldering brass to a copper clad board. A disc of alumina was created by the following serendipitous procedure: a 100 µm hole was drilled in the rhenium and filled with pieces of alumina (Johnson Matthey, 22 μ m mesh), which were then melted, creating a disc of alumina. The disc of alumina jumped out of the hole and landed on the wire in the location shown in Fig. 17b. The thermal emissions from the alumina-covered rhenium show a jump in PMT signal when the alumina melts and becomes trans-

PLEASE CITE THIS ARTICLE AS DOI: 10.1063/5.0171214

356

357

358

359

360

361

363

364

365

(b) (a) (C) (d) 50 µm 3500 Temperature (K) 3000 2500 2000 600 800 1000 1200 800 200 600 1000 100 50 100 150 Time (µs) Time (µs) Time (µs) Time (µs)

FIG. 15. Melting and freezing of iridium samples at $P \approx 1$ atmosphere. (Top) Images of the hot sample on the mirror pinhole during an individual melting experiment. (Bottom) Temperature evolution during multiple heating experiments on each sample. Each heating experiment uses a single pulse. (a,b) The same iridium sample melted in air using (a) the standard 200 mm focal length focusing lens, and (b) a 100 mm focal length focusing lens that lowers the system magnification 2-fold, hence causing the pinhole to appear 2-fold larger in diameter. The outer edges of the images show the texture of un-melted iridium, whereas the central $\sim 100 \ \mu \text{m}$ wide region shows the texture of iridium after melting and refreezing multiple times. (c) A different iridium sample melted in air with a 200 mm focal length lens. The bright spots in the image formed during repeated melting experiments. (d) An iridium sample melted under vacuum. The filtering timescale for (a)-(d) are 40 μ s, 50 μ s, 20 μ s, and 10 μ s.

parent, allowing increased transmission from the Re. After the jump, the temperature evolution is anomalous for a few ms, before rising again. This evolution suggests that the apparent plateau in temperature is caused by the latent heat of melting. Note that it is implausible for the plateau to be caused by a change in the rhenium heater, which is expected to melt 3455 K, and which does not undergo any textural changes visible in white light images. The other side of the rhenium heater also shows a subtle plateau at the same time, a result of the latent heat of melting but with a substantial temperature difference between the other side's surface and the alumina (Fig. 17a). Both sides show plateaus due to the latent heat of freezing with large supercooling, evidenced by 200 K of hysteresis.

Our attempt to reproduce this serendipitous sample preparation, resulted in a much larger pool

PLEASE CITE THIS ARTICLE AS DOI: 10.1063/5.0171214

374

375

376

377

(b) (a) 20 µm (C)Temperature (K) 2000 1800 1600 150 100 Time (µs)

FIG. 16. Melting and freezing of iron under vacuum. Images of the mirror pinhole during melting (a) and in white light after melting (b). (c) Temperature evolution during multiple heating experiments. Each experiment uses a single pulse. The filtering timescale is 10 μ s.

of alumina on one side of the new rhenium heater (Fig. 17c). The alumina side shows a less 366 reproducible jump in PMT signal upon melting, and much less transparent alumina in the heating 367 photos, perhaps because part of the alumina blob did not melt. Still, the alumina side shows a 368 plateau in temperature at 2200 ± 25 K, far below the 2317 K melting temperature of alumina. 369 The discrepancy is likely because emissions from the rhenium undergo wavelength-dependent 370 scattering by grain boundaries in the crystalline regions of the alumina. On the other hand, the 371 clean side of the rhenium heater shows a subtle melting plateau at temperature slightly lower than 372 than 2317 K (Fig. 17c), and a sharp freezing plateau with ~ 50 K of hysteresis. 373

For the final experiment on alumina, we used common equipment for multi-anvil experiments to make a rhenium capsule with 50 μ m-thick rhenium foil, which we stuffed with alumina pieces and closed by crimping and spark welding. We clamped the edges of the rhenium capsule between pieces of 0.5 mm thick Mo foil. The result is an ambient pressure heater and sample with larger mass than the other samples documented here, requiring 100s of ms to heat. It shows clear

PLEASE CITE THIS ARTICLE AS DOI: 10.1063/5.0171214

379

380

381

382

383

384

385

386

387

388

389

390

391

392

393

(b) (c) (d) (e) (a) Temperature (K) 2000 0002 50 60 300 40 40 50 200 150 200 60 150 250 250 Time (ms) Time (ms) Time (ms) Time (ms) Time (ms)

FIG. 17. Melting and freezing of alumina heated by conduction from Joule heated rhenium under vacuum. (Top) Images of the rhenium and alumina on mirror pinholes. White arrows in (a) and (c) point to the edge of alumina blobs. (Bottom) Evolution of color temperature, a proxy for the rhenium temperature. Black arrows point to plateaus caused by melting of alumina. (a,b) A flattened rhenium wire with a disc of alumina on one side of the wire (yellow disc in image (a)). (c,d) A different rhenium wire, flattened, with a pile of alumina on the side in (c). (e) The surface of an rhenium capsule stuffed with alumina. Each experiment uses a single pulse. The filtering timescales for (a)-(e) are 3 ms, 3 ms, 15 ms, 15 ms, and 30 ms.

plateaus upon melting and freezing at temperature slightly lower than the known value of melting temperature of alumina (Fig 17e). The slightly depressed plateau temperatures for rhenium surfaces that are not touching alumina (Fig. 17a-d) are likely caused by temperature gradients between the location on the rhenium that is measured and the molten alumina. Indeed, we document no discrepancy in the one example in which the measured rhenium surface is covered in a disc of fully molten alumina.

Finally, we mention several failed attempts to document accurate melting temperatures using the new MA-PMT system. First, heating tungsten or tantalum in air resulted in plateau temperatures that ranged from 100 to 800 K below the literature values of melting temperature. Second, after nearly 100 repetitions of melting the iridium shown in Fig. 15a,b in air, the color temperature of the plateau decreased by ~ 100 K to 2620 K. We speculate that the anomalies were caused by rapid oxidation of tantalum and tungsten in air, and by the relatively slow oxidation of iridium in air. Third, heating rhenium and tungsten in KCl resulted in depression of plateau temperatures by 300-400 K. In these cases, chemical reaction with KCl or with water absorbed in the KCl could cause the discrepancy by lowering the melting temperature, or by introducing a substantial

PLEASE CITE THIS ARTICLE AS DOI: 10.1063/5.0171214

wavelength dependence of emissivity.

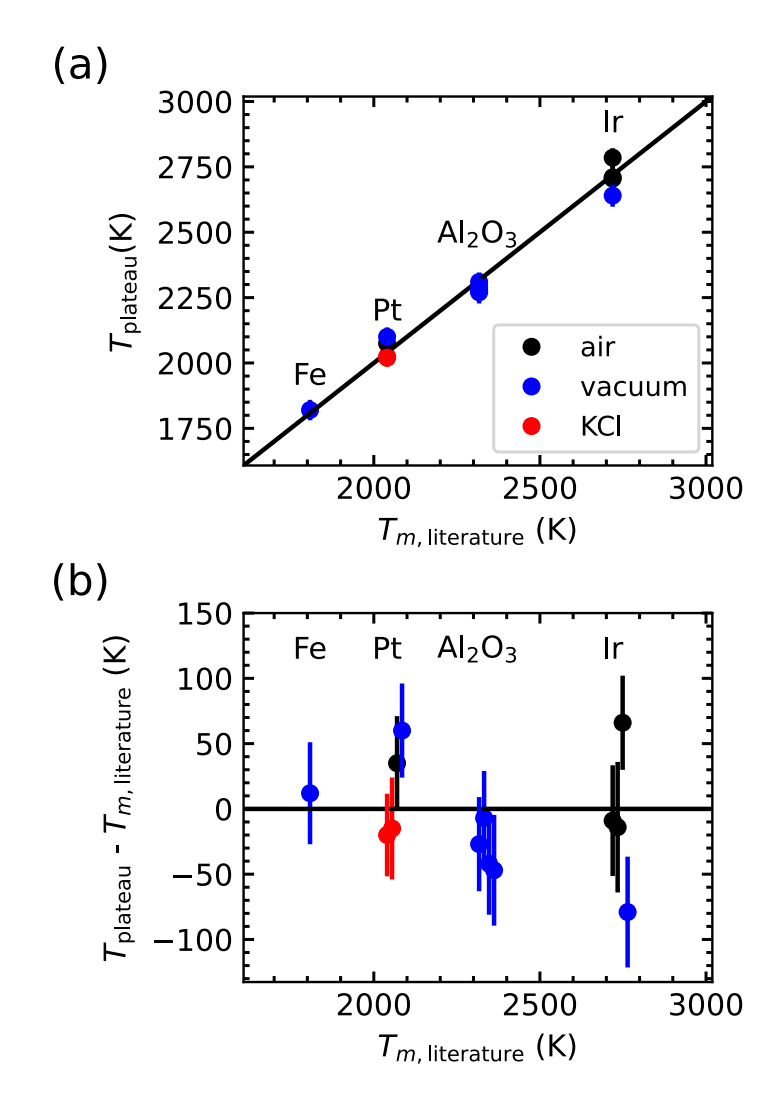


FIG. 18. Summary of the precision and accuracy of temperature measurements at ambient pressure. (a) Measured plateau temperature versus literature value of melting temperature for iron, platinum, alumina, and iridium. Colors indicate the medium in which the sample is heated: air (black), vacuum (blue), or KCl (red). (b) The same data in (a) after subtracting $T_{m,\text{literature}}$. Each symbol and error bar represent the average plateau temperatures and the quadrature sum of two sources of uncertainty: the variation in plateau temperature (i.e. the half-width of the grey shading in Figs. 13-17), and the 30 K uncertainty (1σ) that is typical of two parameter Planck fits in this study.

Fig. 18 summarizes the fifty-five plateaus documented on ten distinct samples in Figs. 12-17.

(We omit the anomalously low plateau temperatures measured when viewing through a large blob

PLEASE CITE THIS ARTICLE AS DOI: 10.1063/5.0171214

412

413

414

415

416

417

418

419

420

421

422

423

424

425

of alumina in Fig. 17c.) Each set of melting experiments (e.g. Fig. 13a) is represented by a single data point in Fig. 18. Note that the measured values of platinum's melting temperature in KCl 398 are slightly lower than for platinum in air or under vacuum. We would expect the opposite trend 399 if the pressure were to increase by ~ 1 GPa during the gentle compression in KCl or during the 400 heating pulse itself, since the slope of platinum's melting curve is 40 K/GPa.8 This suggests that 401 the sample preparation for the samples in KCl resulted in less than ~ 1 GPa of pressure. 402

In all cases, the average plateau temperature measured for a sample is within 80 K of the 403 literature value for melting temperature. This suggests that the accuracy of the temperature mea-404 surement is better than ± 80 K. The rms deviation is 40 K, suggesting a 1σ accuracy of 40 K.

VII. DISCUSSION

The typical precision of the MA-PMT based spectroradiometry system is ± 30 K. The accuracy 407 may be as good as $\pm 40 \text{ K} (1\sigma)$, but a more conservative estimate is the $\pm 80 \text{ K}$ range that encom-408 passes all plateaus documented here. The rise time is 0.24 μ s, but we typically filter to 0.6 μ s for 409 the high pressure data and to 10s or 100s of μ s for the slower heating to lower peak temperatures 410 in our ambient pressure melting tests. 411

The system can be calibrated using common optical tools, plus the tungsten lamp that is a necessary tool for spectroradiometry. The calibrations and temperature fitting procedures are more complicated than the procedures for standard spectroradiometry because of the mediocre spectral resolution of the MA-PMT assembly. Alternative designs with higher spectral resolution are possible. For example, it would be simple to reduce the number of MA-PMT channels per oscilloscope channel from 4 to 1 on the right side's Acton spectrometer, or from 5 to 1 on the left side's Holospec spectrometer. Each change would require more channels on oscilloscopes (or on digitizers), reduce the thermal emissions signal per channel, and allow for a simpler data analysis without the interpolation step – see Appendix D for discussion of when interpolation is needed. For example, the electrical readout design could follow the electrical readout design in Ref. 32, which uses 32 high speed digitizers. The main disadvantages of adding readout channels are the increased system cost and the decrease in signal amplitude per channel (hence decrease in signal-to-noise).

The main result of this manuscript is that MA-PMT assembly can be integrated into a timeresolved spectroradiometry system for DAC experiments. Moreover, the data suggest that the MA-PMT assembly provides a major improvement in signal-to-noise compared to streak cam-

PLEASE CITE THIS ARTICLE AS DOI: 10.1063/5.0171214

446

447

448

449

450

451

452

453

eras. Our implementation of a MA-PMT assembly provides a substantial improvement in signal 427 to noise over our previous work using a streak camera detector, 8 at least at low signal intensity. For 428 comparison, Fig. 10 shows that the MA-PMT-based optical table is capable of measuring precise 429 temperatures down to ~ 1900 K and 2000 K when accumulating 1 and 10 repetitions (lower red 430 and yellow curves), whereas the streak camera-based optical table used in Ref. 8 is capable of 431 measuring precise temperatures down to ~ 2600 and 3000 K (upper red and yellow curves). The 432 difference in temperature corresponds to a factor of 20 in the number of photons measured per 433 second (assuming the system response of the MA-PMT-based optical table), suggesting that the 434 MA-PMT-based system is roughly 20 times more sensitive than the streak camera based system. 435 (Note that we are comparing the sensitivity of the spectroradiometry systems, not of individual 436 channels of the two detectors). Moreover, our MA-PMT-based optical system is has lower chro-437 matic aberration (4.5 mm vs. 8 mm iris diameter, using the same 20x NIR Mitutoyo objective) and 438 higher resolution spatial filtering (5 μ m vs. 12 μ m diameter collection area). 439

The increase in sensitivity opens up major opportunities to study Earth's mantle and core dur-440 ing pulsed heating experiments. For example, thermal conductivity measurements at lowermost 441 mantle conditions may be possible in single-shot mode, eliminating the need for reproducible 442 heating during 100s to 1000s of repetitions (as used in Refs. 2, 10, and 30). Likewise, the im-443 proved sensitivity expands the measurable temperature range during single-shot pulsed heating 444 DAC experiments on chemically reactive samples such as fluid H₂O or H₂. 445

There are two likely causes for the improved sensitivity. First, the much lower number of colors (i.e. much wider bandwidth per pixel) measured in the MA-PMT system reduces noise since each channel of a detector's readout electronics adds its own dark noise. Second, individual PMT channels may have higher quantum efficiency or lower noise than the phosphor detector and multichannel plate that make up the front end of the streak camera. Regardless of the reason, MA-PMT assemblies provide a major improvement in signal-to-noise over the streak camera used in Ref. 8, at least at the low thermal emission intensities achieved with a 2000-3000 K source, 1 to 10 repetitions, and a 0.6 μ s filtering timescale.

Since streak cameras themselves are not a widespread technology in DAC labs, we briefly com-454 pare MA-PMTs and streak cameras with other technologies that are used for spectroradiometry 455 in DACs: iCCDs and sets of single-channel photodiodes or PMTs. The major advantage of a 456 MA-PMT or streak camera over an iCCD is that thermal emissions are measured during a range 457 of times during each pulse, rather than averaging over a single time interval. This means that a accepted manuscript. However, the online version of record will be different from this version once it has been copyedited and typeset PLEASE CITE THIS ARTICLE AS DOI: 10.1063/5.0171214 is the author's peer reviewed,

measurement of temperature at 20 different times requires 20-times more repetitions than needed 459 in a MA-PMT or streak camera system. This is a crucial difference for samples that do not heat 460 and cool reproducibly (e.g. because of shape changes during melting). Moreover, MA-PMTs and 461 streak cameras have two main advantages compared to the sets of single channel detectors used in 462 Refs. 11, 16, 18, 32, 36–38. First, alignment of different wavelengths is trivial since a spectrome-463 ter can focus all wavelengths at the location of the PMT anodes. Second, high throughput of light easy to achieve because of the high efficiency of the spectrometer's grating. In other words, a 465 MA-PMT assembly or streak camera couples well with a spectrometer, enabling the advantages 466 of spectrometers in spectroradiometry. Note that the design in Ref. 32, which has been used for 467 shock wave experiments and not DAC experiments, is intermediate between our design and the 468 design of other systems that use several standalone PMTs with bandpass filters and beamsplitters. 469 The system in Ref. 32 disperses light with a prism-based spectrograph, and collects the dispersed 470 light with an array of thirty two optical fibers coupled to thirty two standalone PMTs. We suspect 471 that the use of a prism and optical fibers complicates alignment and reduces throughput compared 472 to our design, but not nearly as much as the complication and throughput reduction that would be 473 caused by coupling many beamsplitters and bandpass filters to divide thermal emissions into thirty 474 two colors. 475

One limitation of MA-PMT assemblies is that few options are available in the market. For 476 example, we are not aware of any MA-PMT assemblies with sensitivity in the mid-IR spectrum, 477 unlike the single channel detectors used in Ref 18. Another disadvantage of the designs using an 478 MA-PMT assembly plus spectrometer rather than a set of single channel detectors and bandpass 479 filters is that wavelength calibration is trickier. On the other hand, the near linearity of dispersion 480 of modern spectrometers enables the simple calibration routine employed here. In practice, the 481 MA-PMT assembly based system presented here has a much higher time resolution (0.24 μ s rise 482 time) than the single channel detectors used in Ref. 18 (14 µs sampling rate; 5 kHz InGaAs 483 detectors) and Ref. 16 (20 kHz working frequency). 484

85 VIII. CONCLUSIONS

A new optical system for spectroradiometry in pulsed Joule heated diamond cells is presented.

MA-PMT assemblies provide outstanding precision and accuracy for spectroradiometry at \sim 1700 to 2700 K and sub- μ s time resolution while collecting from a 5 μ m-diameter measurement

PLEASE CITE THIS ARTICLE AS DOI: 10.1063/5.0171214

area. The system is compatible with Joule heated DACs. The precision and accuracy of the new system are estimated to be ± 30 K and ± 80 K.

ACKNOWLEDGMENTS

This material is based upon work supported by the National Science Foundation under Grant 492 No. 2125954. We thank Seth Wagner, Vic Lugo, and Cesar Sanchez for machining parts. We 493 thank Amol Karandikar and Joe Lai for fruitful discussions.

DATA AVAILABILITY STATEMENT

The data that support the findings of this study are available at 10.5281/zenodo.10307340.³⁹ 496

Appendix A: Mirror pinhole fabrication

The mirror pinholes were fabricated from broadband-coated glass discs (Edmund Optics 45-498 658). First a piece of platinum wire was pressed to 5 μ m thickness and laser cut into an $\sim 100 \ \mu$ m 499 diameter disc. Next, the disc was placed at the center of the glass disc. Next, a ~ 200 nm-thick 500 layer of aluminum was deposited on the masked optical glass using RF magnetron sputtering. 501 Next, the platinum disc was removed using a micromanipulator. Next, dust was blown off the 502 glass's surface using compressed air. This revealed dozens of $\sim 10-50~\mu m$ wide holes in the 503 aluminum, spaced randomly around the 12.5 mm-diameter piece of glass. Next, the platinum disc 504 was placed in the same location with $\sim 2 \, \mu \text{m}$ accuracy using a micromanipulator. Next, another \sim 505 200 nm thick layer of aluminum was deposited on the re-masked glass disc. After removing the 506 platinum disc and blowing with compressed air, no holes were observed in the deposition, leaving 507 the intentional pinhole as the only hole. However, imperfections are evident in the aluminum coating, such as the small dot above the pinhole in Fig. 9c. The imperfections are the locations 509 that were accidentally masked by dust particles during one of the two depositions, meaning the 510 aluminum is ~ 200 nm thick in those areas.

is the author's peer reviewed,

accepted manuscript. However, the online version of record will be different from this version once it has been copyedited and typeset

PLEASE CITE THIS ARTICLE AS DOI: 10.1063/5.0171214

523

524

525

526

527

529

531

534

535

Appendix B: Linearity of the MA-PMT assembly

We use the 32 channel MA-PMT assemblies from Hamamatsu because the 32-channel version 513 seems to have much larger dynamic range than the 8-channel version. Our testing with 10 μ s 514 duration pulses of LED light suggests that the 8-channel version saturates at $\sim 30 \ \mu A$ anode 515 current regardless of supply voltage, whereas the 32-channel version saturates at 50 to 250 μ A for 516 supply voltage from -500 to -800 V, with saturation current increasing with the magnitude of the supply voltage as expected when the mechanism of saturation is that photoelectron current begins to have a large effect on the voltage of the voltage divider. The \sim 10-fold difference in anode 519 saturation current at high gains effectively gives the 32-channel MA-PMT assembly a 10-fold 520 increase in dynamic range compared to the 8-channel version. 521

The MA-PMT assembly is placed at the spectrometer focus with mediocre accuracy $-\sim 3$ mm 522 accuracy on the Acton spectrometer side (focal length 300 mm), and ~ 10 mm accuracy on the Holospec side (85 mm focal length). Whatever misalignment of the MA-PMT assembly position exists in our system does not noticeably degrade our spectral resolution; shifting the focal position of the detector by 10 mm does not change the sharpness of peaks in our wavelength calibration (Fig. 6). Moreover, the slight misalignment might be beneficial for spreading light over the MA-PMT's photodiodes, because according to Ref. 32, this enhances the range in which the PMT 528 channels have a linear response (Fig. 4. In an attempt to enhance the dynamic range of the MA-PMT assembly on the Acton spectrometer side, we tested the effect of adding an anisotropic 530 holographic diffuser (Edmund Optics 47-999) located 5 ± 2 mm from the PMT photocathodes. The diffuser's high scattering direction was aligned along the height of PMT photocathodes so 532 that at the spectrometer's focal position, the rainbow of light from the 100 μ m diameter pinhole 533 would no longer be focused to its nominal height ($\sim 100 \ \mu m$), but would instead be defocused to \sim 3 mm in height. The measured effect on PMT linearity was negligible, so we removed the diffuser. 536

Appendix C: Electrical pickup from Joule heating pulses

A large pulse of Joule heating current contributes a spurious component to the voltage measured 538 on PMT readout electronics. For example, a 10 A, 100 μ s heating pulse causes a time varying 539 voltage signal of ~ 1 mV amplitude on the left side (e.g. purple curve in Fig. 8a), and 0.2 mV 540

This is the author's peer reviewed,

accepted manuscript. However, the online version of record will be different from this version once it has been copyedited and typeset PLEASE CITE THIS ARTICLE AS DOI: 10.1063/5.0171214

553

554

555

556

557

558

559

560

561

562

563

564

568

on the right side. The signal is relatively slowly varying (10s of μ s period) and nearly equal on each channel (varying by up to $\sim 10\%$). Therefore, in analysis we can eliminate $\sim 90\%$ of this 542

spurious pick-up signal by subtracting the voltages measured on channel 0, i.e. the farthest infrared 543

channel. On the right side, channel 0 is dominated by noise and/or spurious pick-up in all cases.

On the left side, channel 0 is disconnected from the MA-PMT assembly. After collecting the data

for this study, channel 0 of the was also disconnected from the right side MA-PMT assembly for

simplicity. An example of the raw data before and after subtraction is shown in Fig. 8. The 547

spurious signal seems to come from imperfect grounding; by reducing the lengths of each of four 548

key grounding wires from ~ 1 meter to ~ 20 cm, we reduced the pickup amplitude ~ 10 -fold to 549

achieve the results shown here. Specifically, we reduced the lengths of 18 AWG braided wires 550

from left and right oscilloscope grounding pins to left and right MA-PMT assembles, and from 551

MA-PMT assemblies to the optical table. 552

In practice, this pickup problem is only a cause for concern at low temperatures, high currents, and durations longer than $\sim 5 \mu s$, which we use for ambient pressure tests, but not for high pressure experiments. In other words, spurious signal is maximized in our proof-of-concept ambient pressure measurements. Nevertheless, improved design in future MA-PMT-assembly based systems could simplify data collection and analysis. To aid in future designs, note that we observe electrical pickup to be independent of MA-PMT supply voltage in the range 0 V to -900 V and approximately proportional to the amplitude of the Joule heating current pulse. To give intuition, we note that 1.5 to 3 mV pickup corresponds to $\sim 1 \mu A$ current across the 2.5 k Ω shunt resistors, current that is 50 million times smaller than the Joule heating current. In other words, the magnitude of the pickup signal can be explained by 1 out of every 50 million Joule heating electrons traveling from each group of shorted PMT anodes, through a shunt resistor, the common ground, and through the Joule heated sample.

Appendix D: Interpolation and discretization of the system response

We interpolate the tungsten lamp spectrum, V_W , by differentiating the cubic spline of its inte-566 gral: 567

$$V_{\text{W,interp}} = \frac{d}{d\lambda} \left(\text{Spline} \left(\int V_{\text{W}} d\lambda \right) \right)$$
 (D1)

PLEASE CITE THIS ARTICLE AS DOI: 10.1063/5.0171214

580

The result is a continuous function that preserves the integral of voltage in each wavelength band (i.e. $V_{\text{W,interp}}d\lambda = V_{\text{W}}\delta\lambda$ where $\delta\lambda$ is the bandwidth). We use the "interpolate.CubicSpline" function with the option "bc_type = natural" within the scipy library (version 1.9.1) in python. An example of the system response matrix is shown in Fig. 7.

In practice, we discretize λ in steps of \sim 0.8 nm, thereby increasing the density of interpolated wavelengths 100-fold compared to the measured wavelength. To make sure that the numerical implementation is reasonable, we compare best-fit temperatures for different discretizations: 100-fold, 10-fold, 4-fold, 3-fold, 2-fold, and 1-fold increase in λ -resolution. First, we confirm that the "1-fold" case gives the identical result to a simple python code that directly calculates the Planck fit by the using "curve_fit" to find the best fit temperature and emissivity for the standard equation for spectroradiometry:

$$\varepsilon B(T) = \frac{V_{\text{sam}}}{V_{\text{W}}} B(T = 2255 \text{ K})$$
 (D2)

Second, we confirm that at temperatures within 200 K of the calibration temperature of the tung-581 sten lamp, the correction due to interpolation (rather than use of equation D2) is in the range 10-30 582 K, because $\frac{V_{\text{W,interp}}}{B(2255 \text{ K},\lambda)}$ is approximately constant with respect to wavelength. For example, the 583 corrections for the platinum melting data and alumina melting data presented here are typically 584 -20 K and +10 K, respectively. Third, we note that at temperatures ~ 1000 K higher than the cali-585 bration temperature, a mere 3-fold increase in the density of interpolated values of λ is sufficient 586 to achieve within 10 K of the result for 100-fold increase in λ -resolution. Note that this suggests 587 that a MA-PMT-based detector with \sim 3-fold increase in spectral resolution would be sufficient to 588 achieve ~ 20 K precision without interpolation.

REFERENCES

⁵⁹¹ ¹T. Yagi, K. Ohta, K. Kobayashi, N. Taketoshi, K. Hirose, and T. Baba, Measurement Science and Technology **22**, 024011 (2011).

²R. S. McWilliams, Z. Konôpková, and A. F. Goncharov, Phys. Earth Planet. Inter. **247**, 17 (2015).

³S. M. Peiris and T. P. Russell, Journal of Physical Chemistry A **107**, 944 (2003).

⁵⁹⁶ ⁴L. Dubrovinsky, S. Khandarkhaeva, T. Fedotenko, D. Laniel, M. Bykov, C. Giacobbe,

E. Lawrence Bright, P. Sedmak, S. Chariton, V. Prakapenka, A. V. Ponomareva, E. A. Smirnova,

PLEASE CITE THIS ARTICLE AS DOI:

10.1063/5.0171214

- M. P. Belov, F. Tasnádi, N. Shulumba, F. Trybel, I. A. Abrikosov, and N. Dubrovinskaia, Nature 598
- **605**, 274 (2022). 599
- ⁵A. K. Mishra, T. Muramatsu, H. Liu, Z. M. Geballe, M. Somayazulu, M. Ahart, M. Baldini, 600
- Y. Meng, E. Zurek, and R. J. Hemley, Journal of Physical Chemistry. C 122, 19370 (2018). 601
- ⁶M. Zaghoo, A. Salamat, and I. F. Silvera, Phys. Rev. B **93**, 155128 (2016). 602
- ⁷R. S. McWilliams, D. A. Dalton, M. F. Mahmood, and A. F. Goncharov, Phys. Rev. Lett. **116**, 603
- 255501 (2016). 604
- ⁸Z. M. Geballe, N. Holtgrewe, A. Karandikar, E. Greenberg, V. B. Prakapenka, and A. F. Gon-605
- charov, Physical Review Materials 5, 033803 (2021). 606
- ⁹M. Zaghoo, R. J. Husband, and I. F. Silvera, Phys. Rev. B **98**, 104102 (2018). 607
- ¹⁰Z. Konôpková, R. S. McWilliams, N. Gómez-Pérez, and A. F. Goncharov, Nature **534**, 99 608
- (2016).609
- ¹¹M. B. Boslough and T. J. Ahrens, Review of Scientific Instruments **60**, 3711 (1989). 610
- ¹²P. Asimow, in *Treatise on Geophysics (Second Edition)*, edited by G. Schubert (Elsevier, Oxford, 611
- 2015) second edition ed., pp. 393–416. 612
- ¹³L. R. Benedetti and P. Loubeyre, High Pressure Res. **24**, 423 (2004). 613
- ¹⁴L. R. Benedetti, N. Guignot, and D. L. Farber, J. Appl. Phys. **101**, 013109 (2007). 614
- ¹⁵M. J. Walter and K. T. Koga, Phys. Earth Planet. Int. **143**, 541 (2004). 615
- ¹⁶D. Zhang, J. M. Jackson, J. Zhao, W. Sturhahn, E. E. Alp, T. S. Toellner, and M. Y. Hu, Review 616
- of Scientific Instruments 86, 013105 (2015). 617
- ¹⁷P. Beck, A. F. Goncharov, V. V. Struzhkin, B. Militzer, H.-k. Mao, and R. J. Hemley, Applied 618
- Physics Letters **91**, 181914 (2007). 619
- ¹⁸J. M. Montgomery, M. J. Lipp, Z. Jenei, Y. Meng, and W. J. Evans, Review of Scientific Instru-620
- ments **89**, 125117 (2018). 621
- ¹⁹R. S. McWilliams, D. A. Dalton, Z. Konôpková, M. F. Mahmood, and A. F. Goncharov, Pro-622
- ceedings of the National Academy of Science 112, 7925 (2015). 623
- ²⁰V. Bouyer, I. Darbord, P. Hervé, G. Baudin, C. Le Gallic, F. Clément, and G. Chavent, Combus-624
- tion and Flame 144, 139 (2006). 625
- ²¹A. Matsugi, H. Shiina, T. Oguchi, and K. Takahashi, Journal of Physical Chemistry A **120**, 2070
- (2016).627
- ²²A. Matsugi, Review of Scientific Instruments **91**, 054101 (2020).
- ²³V. B. Prakapenka, A. Kubo, A. Kuznetsov, A. Laskin, O. Shkurikhin, P. Dera, M. L. Rivers, and

PLEASE CITE THIS ARTICLE AS DOI:

10.1063/5.0171214

- S. R. Sutton, High Pressure Research 28, 225 (2008). 630
- ²⁴Y. Meng, R. Hrubiak, E. Rod, R. Boehler, and G. Shen, Review of Scientific Instruments 86,
- 072201 (2015). 632
- ²⁵I. Kantor, C. Marini, O. Mathon, and S. Pascarelli, Review of Scientific Instruments **89**, 013111 633
- (2018).634
- ²⁶S. Petitgirard, A. Salamat, P. Beck, G. Weck, and P. Bouvier, Journal of Synchrotron Radiation 635
- **21**, 89 (2014). 636
- ²⁷S. Anzellini, A. K. Kleppe, D. Daisenberger, M. T. Wharmby, R. Giampaoli, S. Boccato, M. A. 637
- Baron, F. Miozzi, D. S. Keeble, A. Ross, S. Gurney, J. Thompson, G. Knap, M. Booth, L. Hud-638
- son, D. Hawkins, M. J. Walter, and H. Wilhelm, Journal of Synchrotron Radiation 25, 1860 639
- (2018).640
- ²⁸Z. Konôpková, W. Morgenroth, R. Husband, N. Giordano, A. Pakhomova, O. Gutowski, 641
- M. Wendt, K. Glazyrin, A. Ehnes, J. T. Delitz, A. F. Goncharov, V. B. Prakapenka, and H.-642
- P. Liermann, Journal of Synchrotron Radiation 28, 1747 (2021). 643
- ²⁹T. Watanuki, O. Shimomura, T. Yagi, T. Kondo, and M. Isshiki, Review of Scientific Instruments 644
- **72**, 1289 (2001). 645
- ³⁰Z. M. Geballe, N. Sime, J. Badro, P. E. van Keken, and A. F. Goncharov, Earth Planet. Sci. Lett.
- **536**, 116161 (2020). 647
- ³¹See www.hamamatsu.com/content/dam/hamamatsu-photonics/sites/documents/ 648
- 99_SALES_LIBRARY/etd/PMT_handbook_v4E.pdf, with no spaces! 649
- ³²W. P. Bassett and D. D. Dlott, Review of Scientific Instruments 87, 103107 (2016). 650
- ³³A. Karandikar, Development of the Flash-heating Method for Measuring Melting Temperatures 651
- in the Diamond Anvil Cell, Ph.D. thesis, Goethe-Universitat, Frankfurt am Main (2006). 652
- ³⁴Y. Akahama and H. Kawamura, Journal of Applied Physics **100**, 043516-043516-4 (2006). 653
- ³⁵A. R. Ubbelohde, *The Molten State of Matter* (John Wiley, Chichester, 1978) p. 454. 654
- ³⁶H. B. Radousky and A. C. Mitchell, Review of Scientific Instruments **60**, 3707 (1989). 655
- ³⁷J. Li, Q. Wu, J. Li, T. Xue, Y. Tan, X. Zhou, Y. Zhang, Z. Xiong, Z. Gao, and T. Sekine, 656
- Geophys. Res. Lett. 47, e87758 (2020). 657
- ³⁸X. Zhou, W. J. Nellis, J. Li, J. Li, W. Zhao, X. Liu, X. Cao, Q. Liu, T. Xue, Q. Wu, and 658
- T. Mashimo, Journal of Applied Physics 118, 055903 (2015).
- ³⁹Z. Geballe, F. Miozzi, C. Anto, J. Rojas, J. Yang, and M. Walter, "Zenodo data: Spectroradiom-660
- etry with sub-microsecond time resolution using multianode photomultiplier tube assemblies," 661

ACCEPTED MANUSCRIPT

Review of Scientific Instruments

AIP AIP Publishing

662

(2023).

This is the author's peer reviewed, accepted manuscript. However, the online version of record will be different from this version once it has been copyedited and typeset.

PLEASE CITE THIS ARTICLE AS DOI: 10.1063/5.0171214

37